PCCP

PERSPECTIVE

View Article Online
View Journal | View Issue

Cite this: *Phys. Chem. Chem. Phys.*, 2026, **28**, 5629

Recent progress on Janus MoSSe for photocatalytic applications

Jonathan Guerrero-Sanchez, *[a] Subhash Sharma, [a] J. I. Paez Ornelas[b] and Do Minh Hoat[cd]

Janus MoSSe has emerged as a promising 2D platform for photocatalytic water splitting owing to its intrinsic out-of-plane dipole, selective surface reactivity, and efficient charge separation. However, pristine MoSSe remains intrinsically limited for the oxygen evolution reaction (OER), which drives the need for structural, chemical, and interfacial engineering. In this perspective, we review recent progress in understanding how defect chemistry, transition-metal functionalization, doping, curvature, and van der Waals heterostructures alter dipole moments, band alignment, carrier lifetimes, and water adsorption energies—all key physical descriptors governing catalytic performance. An interesting picture emerges: MoSSe becomes an effective photocatalyst when paired with an OER-active partner that complements its strong HER-driving conduction band. Connecting it with 2D materials like WS_2, black phosphorus, GaN, and AlN introduces the necessary valence-band depth and polarization to meet both redox requirements. The experimental MoSSe/GaN system supports the theoretical predictions and adds multifunctional Rashba–Dresselhaus spin splitting and magnetic-field-enhanced charge dynamics to the list of photocatalytic descriptors. Collectively, these insights lay out a design roadmap for engineering Janus-based heterostructures that optimize water splitting under visible light.

Received 8th December 2025,
Accepted 2nd February 2026

DOI: 10.1039/d5cp04758g

rsc.li/pccp

1 Introduction

Transition metal dichalcogenide monolayers (TMDs) have the well-known MX_2 formula, where M is a transition metal—most commonly Mo and W, while X represents a chalcogen species, typically S, Se, and Te. For a long time, these 2D materials have been among the most compelling platforms in materials science due to their versatility and wide range of applications.[1–3] These structures are easily exfoliated because, in their bulk counterparts, they are held together by weak van der Waals forces, while in-plane, they exhibit strong covalent bonds.[4,5] 2D TMDs, especially MoS_2 and WS_2 and their Se counterparts, usually display direct band gaps, large exciton binding energies, spin-valley locking, and spin–orbit coupling in the W variants, among other properties.[5,6] These intriguing phenomena arise from d–p hybridizations between the constituents, with d orbitals from the transition metal and p orbitals from the chalcogen atoms.

Furthermore, these properties can be tuned through different methods, such as controlling composition, creating different stacking configurations, applying strain, external fields, and doping.[4,7] In terms of applications, TMDs span a broad spectrum from transistors, photodetectors, and solar cells to electrocatalysis, memory devices, and flexible electronics.[8,9] Yet, challenges remain in improving their performance. A way to achieve this is by building heterostructures, defect engineering, alloying, and symmetry breaking.[2,10] The last one has been the focus of the scientific community, resulting in the development of the asymmetric Janus counterparts, a new class of materials from the TMD family with tailored properties due to the existing charge density asymmetry in their layers.

This class of TMDs has gained attention since their successful synthesis.[11,12] The main characteristic in these layers is the broken out-of-plane mirror symmetry. Structurally, the transition metal is sandwiched between two different chalcogens, usually S, Se, and Te. Recently, O has been included in this combination. The generated vertical asymmetry induces novel properties, such as an electric dipole, which enables spontaneous charge polarization, Rashba spin splitting, and piezoelectricity, among others.[5,10] Janus TMDs are also an ideal platform to explore magnetic effects in two dimensions.[6,7] Additionally, the different orbital hybridization in the chalcogen layers enhances their sensitivity, making them applicable in surface catalytic processes and sensing.[2]

[a] *SECIHTI – IxM - Centro de Nanociencias y Nanotecnología, Universidad Nacional Autónoma de México. Km 107 Carretera Tijuana-Ensenada, AP 14, Ensenada B.C., 22860, México. E-mail: guerrero@ens.cnyn.unam.mx*
[b] *Facultad de Ciencias, Universidad Autónoma de Baja California, Ensenada, Baja California, 22860, Mexico*
[c] *Institute of Theoretical and Applied Research, Duy Tan University, Ha Noi, 100000, Vietnam*
[d] *School of Natural Sciences, Duy Tan University, Da Nang, 550000, Vietnam*

In this perspective, we focus on the MoSSe monolayer, as it is the first to be synthesized and the most widely used among the Janus class. We highlight how structural asymmetry, interface design, and chemical modifications engineer its properties, unlocking the MoSSe potential for photocatalytic water splitting.

2 Growth techniques

In 2017, the first report of MoSSe growth was published,[12] where researchers prepared single-crystalline triangular molybdenum disulfide (MoS_2) monolayers on c-plane sapphire substrates through chemical vapor deposition. Then, the top chalcogen layer was replaced with hydrogen atoms using hydrogen plasma, followed by a further step where thermal selenization was used to replace the hydrogen atoms.[12] Since then, Janus monolayers have been a topic of great interest to the scientific community, although the synthesis of these monolayers represents a challenge due to the selective process involved, namely replacing just one layer of the structure without disrupting the other layers or the lattice integrity. Some approaches adopt a two-step post-synthesis substitution strategy, where MoS_2 or $MoSe_2$ is fabricated using chemical vapor deposition, followed by top-layer replacement *via* hydrogen-plasma-assisted sulfurization[13–15] (Fig. 1a), or selective sulfurization/selenization, typically with controlled annealing[16–18] (Fig. 1b). Additionally, large-area, uniform Janus monolayers have been recently developed using vertically aligned CVD flow systems. This design exposes metallic Mo or MoX_2 (X = chalcogen) films supported on an Au substrate to S and Se precursors to form wafer-scale Janus layers, which are highly reproducible and scalable.[19,20]

Other strategies, distinct from CVD, have emerged, enabling easy one-pot hydrothermal synthesis of MoSSe. Mo, S, and Se precursors with a molar ratio of 1 : 1 : 1 are used. The process starts with sodium molybdate added to a beaker containing distilled water, and in another beaker, L-cysteine is combined with distilled water. Both solutions are sonicated and mixed, then selenium powder is added, followed by ascorbic acid. The mixture is sonicated again for 10 minutes. HCl is then added to the resulting solution, which is placed in an autoclave and subjected to hydrothermal synthesis at 200 °C for 20 hours. This results in Janus MoSSe nanoflowers.[21] Fig. 1c illustrates a schematic representation of the growth procedure.

3 Conditions for a promising photocatalyst

The photocatalytic H_2O splitting into H_2 and O_2 is driven by photogenerated electrons and holes in a semiconductor whose band edges straddle the redox potential of both reactions (0 V and 1.23 V *vs.* RHE (reversible hydrogen electrode)). The light-induced process is driven by one-step and two-step excitations. The one-step excitation occurs when a single photocatalyst can absorb photons with energies above the semiconductor band gap (it should be larger than 1.23 eV) and both charge carriers reach active sites without excessive recombinations, as seen in Fig. 2a.[22] In contrast, the two-step process or Z-scheme (Fig. 2b) uses a couple of semiconductors connected through electron mediators, each taking care of one half reaction (H_2 and O_2 formation). This type of arrangement enables absorption in the visible light spectrum, allowing the use of semiconductor materials with narrower band gaps than those used in the one-step process, while still carrying out both redox processes.[22,23] This energetic alignment was first established in 1972[24] by Fujishima and Honda, who demonstrated that the oxygen evolution reaction (OER) occurs anodically and the hydrogen evolution reaction (HER) takes place at the cathode. According to Chen, Takata and Domen,[25] appropriate photocatalysts must satisfy the following criteria: (i) they should have appropriate band energy (from 1.8 to 2.4 eV, visible light) and absolute band-edge positions that straddle the water-redox potentials; (ii) high crystallinity to suppress the electron–hole recombination; (iii) strong light absorption and long carrier diffusion lengths; and (iv) chemical stability against photocorrosion in aqueous media. Band alignment and built-in electric fields are essential descriptors for photocatalytic water splitting; however, by themselves, they are not sufficient to guarantee

Jonathan Guerrero-Sanchez

Jonathan Guerrero Sánchez is a Full Professor at the Centro de Nanociencias y Nanotecnología (CNyN) of the Universidad Nacional Autónoma de México (UNAM). He earned his PhD in Materials Science from the Benemérita Universidad Autónoma de Puebla, specializing in the atomic-scale understanding of transition metal structures on semiconductor surfaces. Since joining CNyN, Dr Guerrero Sánchez has established a multidisciplinary research program focused on first-principles simulations of materials for spintronic, catalytic, energy, and environmental applications. His work centers on understanding the effects of defects, surface functionalization, and quantum phenomena in two-dimensional systems such as transition metal dichalcogenides (TMDs), Janus monolayers, MXenes, and layered oxides. A specific focus of Dr Guerrero Sánchez's research is the exploration of novel magnetic states, including magnetodielectric coupling and altermagnetism, and the engineering of electronic, magnetic, and transport properties via surface and defect manipulation. His studies employ density functional theory (DFT), electronic structure analysis, and machine learning strategies to accelerate materials discovery. Dr Guerrero Sánchez has authored over 250 peer-reviewed publications and actively contributes as editorial board member and as a reviewer for leading journals in materials science and physics. In recognition of his contributions, he was selected as a 2024 Rising Star in Materials Science by ACS Materials Au.

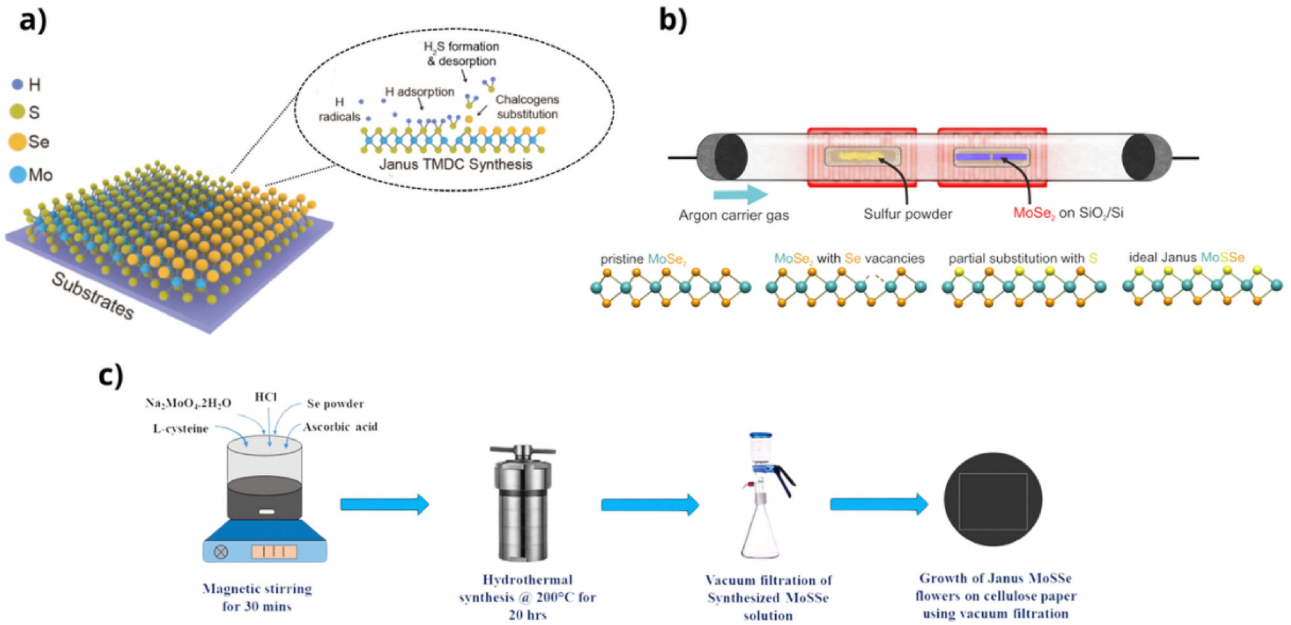

Fig. 1 (a) Schematic illustration of hydrogen plasma-assisted sulfurization of $MoSe_2$ *via* chemical vapor deposition (CVD). The process promotes H_2 formation and Se abstraction, enabling controlled substitution with S atoms to produce Janus TMD layers. (b) Sequential steps in the annealing-based substitution of Se with S, showing pristine $MoSe_2$, Se vacancies, partial S substitution, and ideal Janus MoSSe configuration. (c) One-pot hydrothermal synthesis of MoSSe using Mo, Se, and S precursors. The process involves magnetic stirring, hydrothermal reaction at 200 °C, filtration, and film growth on cellulose substrates. (a) Reprinted and modified from Fig. 1a in the manuscript *ACS Nano*, 2025, **19**, 20744–20752 with permission of the American Chemical Society, (b) reprinted from Fig. 1a in the manuscript *npj 2D Mater. Appl.*, 2024, **8**, 67 under Creative Commons CC BY licence, and (c) reprinted and modified from the scheme in Fig. 1 in the manuscript *Flex. Print. Electron*, 2021, **6**, 015011 with permission from the Institute of Physics Publishing Ltd.

overall activity. In particular, satisfying redox straddling conditions does not ensure that all reaction steps proceed with favorable thermodynamics or accessible kinetics. Although improvements in electronic alignment may drive the completion of the catalytic cycles, it is necessary to explicitly evaluate reaction intermediates and rate-limiting steps to complement electronic descriptors.

4 The photocatalytic potential of MoSSe

Beyond the general criteria required for photocatalytic water splitting, Janus MoSSe exhibits a unique electronic structure that intrinsically induces charge separation and enhances its activity.[26] Its broken out-of-plane symmetry induces a vertical dipole that, as shown by Fu *et al.*,[27] spatially splits the valence and conduction band charge densities across the S- and Se-terminated layers (Fig. 2c). Such polarization results in longer carrier lifetimes than in pristine counterparts. The experimental values are: 100 ps (MoS_2), 125 ps ($MoSe_2$), and 134 ps (MoSSe), which evidences that the vertical dipole (rather than the band gap) is a dominant factor in controlling the recombination dynamics.[27] Another piece of evidence established in Fu *et al.*[27] was that the lifetime scales linearly with the dipole magnitude under strain. Therefore, the Janus MoSSe could be utilized in photocatalysis on its own. Still, it has the potential for improvement when modified with other external factors, such as strain, doping, or the creation of heterostructures with other promising materials.

A more detailed picture of the connection between the electronic structure and interfacial water chemistry is analyzed in the work by Ma *et al.*,[28] which demonstrated that the broken symmetry in the Janus MoSSe structure generates a vertical electrostatic potential drop of 0.78 eV. This built-in field confirms the spatial separation of the valence band maximum (VBM) and conduction band minimum (CBM), efficiently localizing holes on the S side and electrons on the Se side (see Fig. 2c), resulting in a segregation of the oxidative (preferred for the OER) and reductive (preferred for the HER) sites. They also showed that H_2O binds through van der Waals forces and with an adsorption energy 0.04 eV stronger in Janus MoSSe compared to MoS_2. This adsorption preference is induced by the dipole formed in the monolayer.[28]

Digging into the most explicit thermodynamics of the H_2O decomposition, Lie *et al.*[29] computed the adsorption energies of all key intermediates (H, OH, O, O_2, H_2O_2) on both S- and Se-terminated layers of MoSSe. The analysis reveals selectivity towards the HER on the Se-terminated face, with H and H_2 formation exhibiting lower energy barriers, which agrees with the CBM electronic states accumulation on the Se-side, while the OER, which may happen in the S-side, is strongly limited due to potential O–O bond cleavage (energy of adsorbed O is 1.07 eV more stable than O_2 on the S-side), thus hindering recombination into O_2 during the OER cycle.[29] This behavior reflects a broader and recurring limitation of pristine Janus

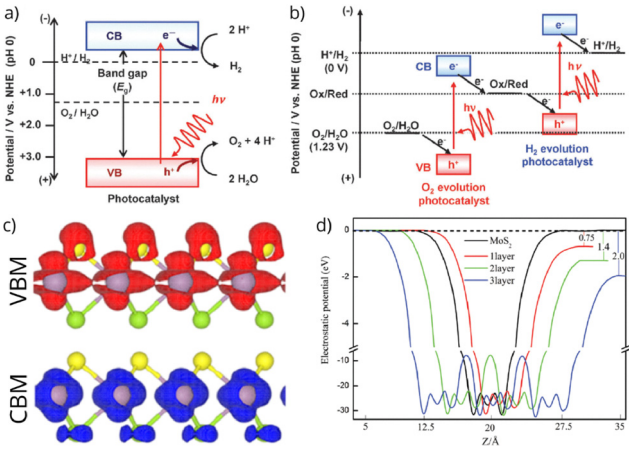

Fig. 2 (a) One-step photocatalytic water splitting scheme illustrating the alignment of the valence band (VB) and conduction band (CB) edges of the photocatalyst with the redox potentials for hydrogen and oxygen evolution reactions. (b) Two-step excitation or Z-scheme photocatalytic process, showing charge transfer between oxygen evolution and hydrogen evolution photocatalysts under light irradiation. (c) Spatial distribution of the valence band maximum (VBM) and conduction band minimum (CBM) for the Janus MoSSe monolayer, highlighting the asymmetric charge localization induced by the Janus structure. (d) Electrostatic potential profiles along the out-of-plane (z) direction for MoS_2 and mono-, bi-, and trilayer Janus MoSSe, showing the increasing built-in electric field with layer thickness. (a) and (b) Reprinted from Fig. 2a and b in the manuscript *Chem. Soc. Rev.*, 2014, **43**, 7520, with permission from the Royal Society of Chemistry; (c) reprinted and modified from Fig. 2c in the manuscript *Nano Lett.*, 2024, **24**, 6425–6432 with permission from the American Chemical Society; and (d) reprinted from Fig. 2d in the manuscript *J. Mater. Chem. C*, 2018, **6**, 1693 with permission from the Royal Society of Chemistry.

MoSSe. While its intrinsic out-of-plane dipole efficiently separates photogenerated carriers and favors the hydrogen evolution reaction, it remains unable to complete the full H_2O splitting cycle. In particular, the oxygen evolution reaction is not completed on the S-side, even in cases where band-edge energetics appears suitable.[29] As a result, pristine MoSSe exhibits an asymmetric catalytic response, underscoring the need for targeted engineering strategies that selectively enhance hole-driven oxidation while preserving its intrinsic HER activity.

In this sense, it was demonstrated that the dipole in the monolayer, 0.037 eÅ with 0.75 eV electrostatic potential difference between S and Se surfaces, can be engineered to 0.072 eÅ in the bilayer and to 0.11 eÅ in trilayers, as well as with an interfacial potential drop of 2.00 eV, see Fig. 2d.[30] The band gap of the monolayer (2.14 eV) is also modified in the range from 0.91 to 1.21 eV for the most stable bilayer (SMoSe/SMoSe). At the same time, for a trilayer, it is 0.7 eV, and it continues to decrease systematically as the number of layers increases.[31] In terms of carrier mobilities, it increases as well from 73.8 $cm^2\ V^{-1}\ s^{-1}$/157.2 $cm^2\ V^{-1}\ s^{-1}$ (e/h) in the monolayer to 1194 $cm^2\ V^{-1}\ s^{-1}$/2915.6 $cm^2\ V^{-1}\ s^{-1}$ (e/h) in the bilayer, and the hole mobility up to 5894 $cm^2\ V^{-1}\ s^{-1}$ in trilayers.[30] Another interesting detail is that for Janus MoSSe multilayers, the VBM and CBM localize on the opposite outer layers, as in the case of the single layer, separating the oxidative and reductive surface reactions.[30] Modulating the thickness of Janus MoSSe provides a controllable route to engineer key electronic descriptors that are important for photocatalysis. However, their explicit improvements need to be tested by calculating the free energies of H_2O and all intermediates.

5 Defect engineering of Janus MoSSe

In terms of defect engineering, it has been observed that modifying the reactivity of Janus MoSSe can be achieved by locally altering the electronic structure and thermodynamic activation. In terms of adsorption energy, H_2O binds weakly to the S-side of MoSSe (E_{ads} −0.243 eV), while mainly preserving the molecular features, without evident O–Mo/S hybridization.[32] Upon introducing an S vacancy, the adsorption energy stabilizes by 0.078 eV; still, the water dissociation is thermodynamically unfavorable, depicting positive adsorption energies of the constituents (H* + OH*) and a larger reaction barrier (1.31 eV).[32] A different effect is observed when considering Mo-related defects. Mo anti-site and Mo interstitial defects create undercoordinated Mo centers with strong O–Mo hybridization, resulting in the loss of molecular features in the projected densities of states.[32] The strong hybridization yields large adsorption energies (ranging from −1.06 to −1.42 eV) and lowers the water splitting barrier to approximately 0.70 eV, which favors water dissociation (H* + OH*) by −0.21 eV and −0.99 eV for Mo antisites and Mo interstitials, respectively (Fig. 3a).

Engineering with transition metals was also analyzed, and it was found that it profoundly reshapes the electronic descriptors and the interfacial chemistry of the Janus MoSSe, all in light of overcoming the weak interaction that H_2O presents in pristine monolayers. The treated metals were Sc, Ti, V, Cr, Mn, Fe, Co, Ni, and Cu.[33,34] In terms of adsorption energies, almost all the 3d TMs present a strong chemisorption on both sides of the Janus MoSSe monolayer; the only TM atom that lies out of the trend is Zn, whose adsorption energy is lower than −0.26 eV. The strong interaction generates shorter TM–S/Se bonds, leading to strong electronic hybridizations.[33] The TM adsorption modifies the intrinsic dipole (0.78 eV in pristine MoSSe) following a clear trend. On the S side, it decreases almost linearly from around 0.6 eV for Ni to approximately −0.6 eV for Sc (Fig. 3b). In sharp contrast, the TMs adsorbed on the Se side generate a dipole increase from Ni (0.9–1.0 eV) to Sc (1.6 eV) (Fig. 3c). Then, on the Se side, charge separation of the photogenerated carriers and surface-selective redox activity may enhance their photocatalytic performance.[33] A redox-level analysis showed that the TM-modified Se side of the Janus MoSSe exhibits proper alignment for both the HER and OER. TM adatom adsorption also extends the optical absorption into lower energies, with coefficients exceeding $10^4\ cm^{-1}$. Notably, Sc, Ti, V, and Cr improve the visible-light harvesting.[33] Another critical and interesting finding was that TM adsorption generates H_2O chemisorption for both S- and Se-sides, with the adsorption energy values for the Se-side going from 0.6 eV to 1.2 eV (see Fig. 3d). On this side, the O atom binds directly atop

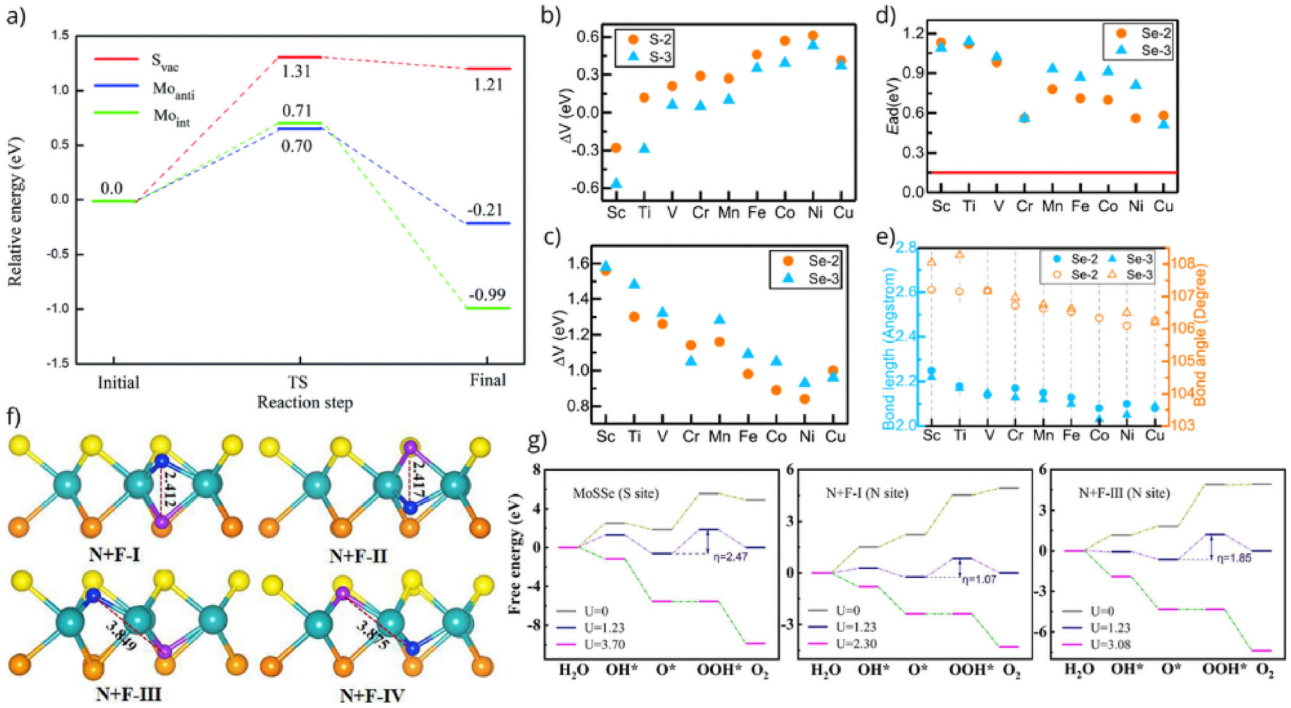

Fig. 3 (a) Reaction energy pathway for the transformation of H_2O to H and OH adsorbed on Janus MoSSe with different intrinsic defects, (b) electrostatic potential difference for different transition metals adsorbed on the S-side of Janus MoSSe, (c) same as (b) but with transition metals adsorbed on the Se-side, (d) evolution of the adsorption energies of H_2O atop different transition metals adsorbed on Janus MoSSe, (e) evolution of the TM–O bond lengths and H_2O angles when adsorbing H_2O atop different transition-metal-decorated Janus MoSSe monolayers, (f) atomistic N + F co-doping models in Janus MoSSe, and (g) OER free energy diagrams at different potentials for the most probable intermediates adsorbed on the Se side of the Janus MoSSe monolayer. (a) Reprinted from Fig. 6 in the manuscript *RSC Adv.*, 2020, **10**, 10816 with permission from the Royal Society of Chemistry and under Creative Commons CC BY licence; (b) and (c) reprinted and modified from Fig. 2 in the manuscript *J. Phys. Chem. C*, 2019, **123**, 18347–18354 with permission from the American Chemical Society; (d) and (e) reprinted and modified from Fig. 5b and 7b in the same manuscript; and (f) and (g) reprinted and modified from Fig. 1c and 8b–d in the manuscript *Appl. Surf. Sci.*, 2021, **544**, 148741 with permission from Elsevier Scientific Publisher.

of the TM atom at distances <2.25 Å and the bond angles increasing by >2 degrees depending on the adsorbed TM atom, as seen in Fig. 3e, signaling H_2O activation and O–TM hybridization.[33]

The co-doping strategy has also been applied, with N + F-*co*-doped MoSSe structures shown to be thermodynamically stable.[35] The N–F treated models are: N + F-1 (N on S side, F on Se side, N atop of F), N + F-II (N on Se side, F on S side, F atop of N), N + F-III (N on S side, F on Se side, N diagonal to F), and N + F-IV (N on Se side, F on S side, F diagonal to N), see Fig. 3f. In these models, the band gap ranges from 1.28 to 1.57 eV, while maintaining the built-in potential difference on the Janus lattice (0.7–0.79 eV),[35] thereby retaining efficient charge separation. An interesting point emerged here: in co-doped systems with N and F, the electronic band structure retained semiconducting behavior across all models, without spin-polarized states or electronic traps appearing. It also enhances ultraviolet visible-light absorption.[35] In terms of Gibbs free energy (ΔG_{H^*}), the ΔG_{H^*} for pure MoSSe at Se sites is 2.04 eV, the ΔG_{H^*} for Se sites at the N + F co-doped monolayer remains larger than 1.70 eV, and ΔG_{H^*} for the N dopant in the Se site in models II and IV is -0.04 eV and -0.11 eV, respectively, the latter values implying that the co-doped MoSSe in configurations II and IV may possess higher HER activity than the pristine Janus MoSSe monolayer Fig. 3g.[35] In the case of the OER, the potential-determining step (from O* to OOH*) is reduced from 3.70 eV in pristine MoSSe to 2.30 eV and 3.08 eV in the N site of N + F models, reflecting improved but still insufficient oxidation kinetics. This strategy highlights that heteroatom pairs systematically modify the physical descriptors that are key to overcoming the fundamental limitations of Janus MoSSe for its broader photocatalytic applications.

6 Morphological effects on MoSSe

The intrinsic Janus asymmetry of MoSSe introduces a built-in dipole perpendicular to the 2D plane, which can be further modulated by inducing curvature in the system. Recent studies have shown that rolling up Janus monolayers into 1D nanotubular structures not only preserves the polarity but also amplifies interfacial electric fields across the tube walls, opening new pathways to manipulate redox site separation and surface reactivity.[36,37]

The MoSSe single-walled nanotubes (SWNTs) can be roughly classified into two limiting chiralities: armchair (n,n) and zigzag $(n,0)$, defined by the direction in which the Janus monolayer is rolled up. These notations are not merely geometric—they

are directly linked to the resulting electronic, mechanical, and surface properties of the nanotube. The rolling vector determines how the broken symmetry of the Janus sheet is projected into the radial and axial directions, thus affecting the distribution of the internal dipole and strain energy.

In armchair (*n*,*n*) configurations, the rolling occurs along the zigzag direction of the monolayer, aligning the Janus asymmetry (S/Se vertical separation) tangentially along the circumference. This configuration produces a well-distributed curvature that reduces localized stress, making these nanotubes energetically more stable than their zigzag counterparts. In contrast, zigzag (*n*,0) nanotubes involve rolling along the armchair direction, which aligns the Janus axis parallel to the tube axis, resulting in more anisotropic curvature and larger strain energy accumulation across the wall.[37]

Furthermore, the curvature affects how the monolayer's intrinsic dipole transforms upon rolling. In planar Janus structures, the dipole is oriented perpendicular to the plane, whereas in nanotubes it is bent into a radial configuration. The direction and magnitude of this radial dipole depend on both the curvature (tube diameter) and the exterior termination. It has been shown that Se@out configurations—where Se atoms occupy the outer surface—are energetically more favorable than S@out ones. This is attributed to Se's larger atomic radius, which mitigates curvature-induced stress when placed externally. Moreover, this configuration localizes the conduction band minimum (CBM) at the Se-terminated surface, facilitating the HER, while the valence band maximum (VBM) remains on the S side, enhancing the OER selectivity at the inner wall.[37]

The curvature-induced polarization plays a pivotal role in enabling charge separation and tuning redox site localization. In Se@out armchair nanotubes, the asymmetry of the Janus monolayer bends into a radial electric field that naturally drives electrons toward the Se-rich outer surface and holes toward the S-terminated inner wall. This spatial separation reduces recombination, as demonstrated in the work by Fu *et al.*, where a remarkably long carrier lifetime of 7.1 ns was reported—an order of magnitude improvement over flat monolayers.[36] This implies that curvature alone, without the need for external fields or interface engineering, can significantly enhance photocatalytic efficiency.

In addition to charge separation, the optical response of these nanotubes aligns favorably with the solar spectrum. Both studies report strong absorption in the visible range, particularly from 500 to 700 nm, owing to curvature-enhanced electronic transitions.[36,37] This absorption is not only broad but also tunable through diameter control: smaller diameters induce larger band gaps due to quantum confinement, while wider tubes present reduced gaps and enhanced light-harvesting capability.

The radial dipole inherent to these curved Janus structures is also tunable. By varying the tube radius, Zhang *et al.* demonstrated a continuous modulation of the dipole strength and the associated electrostatic potential drop across the tube wall.[37] This tuning directly impacts surface reactivity. For example, the hydrogen adsorption free energy (ΔG_{H^*}) decreases significantly with enhanced curvature and polarization, reaching values around 0.38 eV for optimal diameters—an appreciable shift from the unmodified monolayer. While this is still above the ideal thermoneutral value ($\sim$0 eV), it represents substantial progress and highlights curvature as a strategy to approach HER-optimized surfaces.

Structurally, these nanotubes are dynamically stable across a wide range of diameters, and their energetic profiles suggest favorable formation pathways, especially for armchair configurations. The Se@out geometry not only minimizes strain but also aligns favorably with the electronic structure, creating regions of spatially selective reactivity that correlate with redox needs. Notably, the band edges of the MoSSe nanotubes straddle the redox potentials for water splitting under standard conditions, ensuring thermodynamic viability for full H_2 and O_2 evolution reactions.[36]

These findings reveal that MoSSe nanotubes offer a morphologically tunable platform where chirality, curvature, and compositional asymmetry intersect to enhance photocatalytic properties, including dipole moment, charge separation, band alignment, and surface reactivity.

7 MoSSe-based heterostructures and interfacial polarization

In this section, we will dig into type-II band alignment heterostructures – where electrons and holes separate but lose part of their redox driving force – and also the Z-scheme configuration, in which the higher conduction band maintains strong reducing electrons, and the deeper valence band maintains strong oxidizing holes, facilitating the complete H_2O splitting process.

The design of MoSSe/WSSe lateral heterostructures, in which the Janus sheets connect along zigzag boundaries, forms an atomically continuous Mo–W framework with a formation energy of −0.159 eV and a band gap 1.58 eV.[38] Since both monolayers have intrinsic out-of-plane dipoles, the junction develops a pronounced interfacial polarization with a dipole moment reaching 0.873 D and an electrostatic potential drop of 0.089 eV across $\sim$10 Å, establishing synergistic in-plane and vertical electric fields able to separate carriers across the interface.[38] It also shows a charge-transfer of 0.222*e* from WSSe to MoSSe, helping suppress recombination. In terms of band alignment, the heterostructure presents a type-II alignment with the CBM on MoSSe and the VBM on WSSe (see Fig. 4a), yielding favorable driving forces for the HER and OER with the CBM above the reduction level of hydrogen by 0.141 eV, and the VBM is lower than the oxidation potential by 0.207 eV under acidic conditions, as seen in Fig. 4b.[38]

The free energy values obtained for hydrogen adsorption at the MoSSe and WSSe sides are 1.74 eV and 1.81 eV (similar to those found in the separated counterparts), respectively. Still, the WSSe side provides a high hole mobility of 3274.5 $cm^2\ V^{-1}\ s^{-1}$, which may enable efficient hole transport towards the oxidation

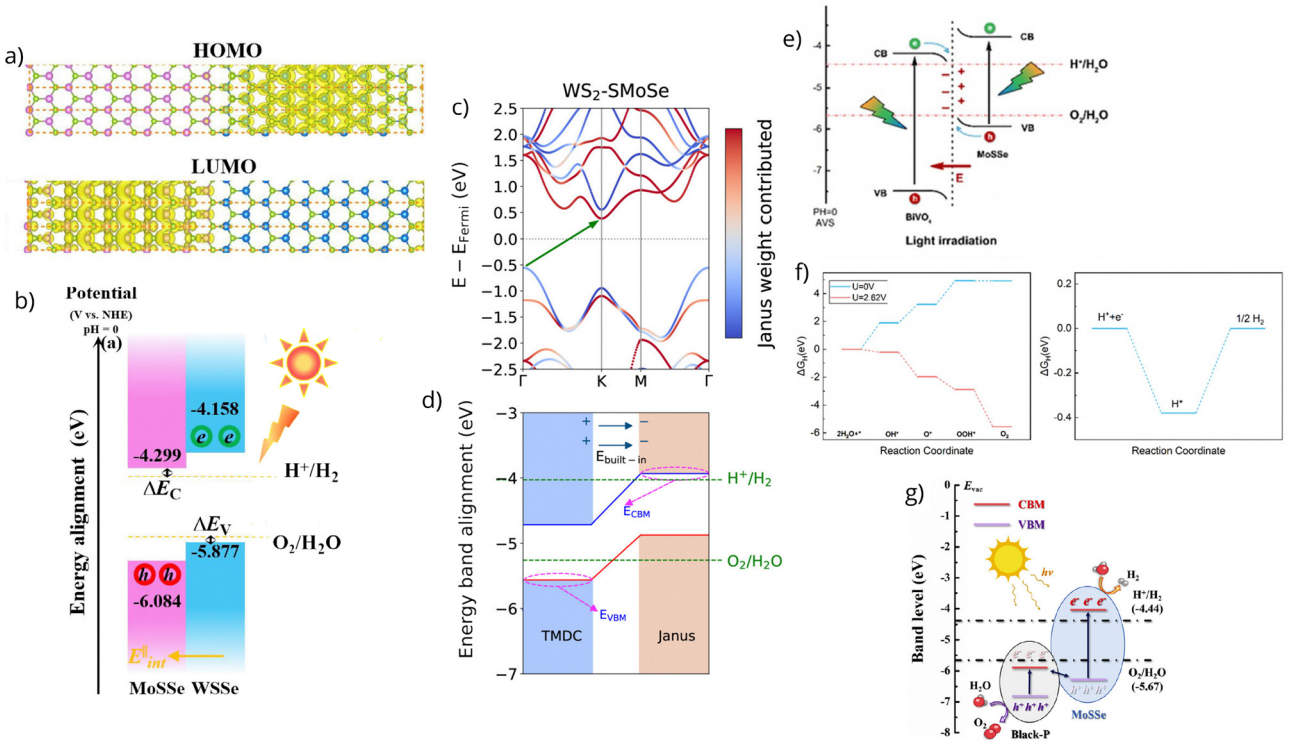

Fig. 4 (a) Highest occupied molecular orbital (HOMO) and lowest unoccupied molecular orbital (LUMO) charge density distributions for the MoSSe|WSeS heterostructure, indicating charge localization and potential sites for charge transfer. (b) Energy level alignment diagram for the MoSSe|WSeS lateral heterojunction relative to the vacuum level, showing conduction and valence band positions relevant to photocatalysis. (c) Band structure of the WS_2|MoSSe heterostructure at the HSE level, with Janus-layer contributions highlighted *via* color mapping. (d) Energy band alignment at pH = 7 for TMDC–Janus heterostructures, showing a built-in electric field ($E_{built-in}$) promoting charge separation. (e) Band alignment of the MoSSe|$BiVO_4$ heterostructure under illumination, positioning the bands for redox compatibility. (f) Gibbs free energy diagrams for water oxidation (left) and hydrogen evolution (right) reactions at various applied potentials in the MoSSe|$BiVO_4$ system. (g) Band alignment of the black-P|MoSSe heterostructure under light irradiation, showing the generation and separation of photoinduced charge carriers. (a) and (b) reprinted and modified from Fig. 5a, b, and 9a in the manuscript *J. Catal.*, 2021, **404**, 18–31 with permission from Elsevier; (c) and (d) reprinted and modified from Fig. 2 (left upper and lower panels) in the manuscript *ACS Appl. Energy Mater.*, 2025, **8**, 5209 with permission from the American Chemical Society under CC-BY-NC-ND 4.0 license; (e) and (f) reprinted and modified from Fig. 7d and 8 in the manuscript *J. Phys. D: Appl. Phys.*, 2022, **55**, 305501 with permission from IOP Publishing; and (g) reprinted from Fig. 6a in the manuscript *Int. J. Hydrogen Energy*, 2021, **46**, 39183 with permission from Elsevier scientific publisher.

sites. At the same time, the full heterostructure maintains an optical absorption exceeding 105 cm^{-1} across NIR-UV.[38]

When coupling Janus MoSSe with an OER-active monolayer, WS_2, the vdW heterostructure presents an indirect HSE gap of 0.94 eV (see Fig. 4c). However, it still generates a built-in potential difference (0.79 eV) originating from the dipole, which increases the effective Z-scheme energetic bias to 1.72 eV, ensuring that the MoSSe CBM and MoS_2 VBM straddle the H^*/H_2 and O_2/H_2O redox levels (Fig. 4d).[39] The interface polarization provided by MoSSe and the stabilized valence band by WS_2 help retain the reducing electrons in MoSSe and the oxidizing holes in WS_2, a hallmark of a productive Z-scheme. A proof of that is its excellent solar-to-hydrogen efficiency of 16.62% at pH = 7, with a small hydrogen overpotential (χ_H) of 0.09 eV and a moderate oxygen overpotential χ_O of 0.39 eV. It also shows a high visible-light absorption efficiency of 88.54% and an in-plane absorption coefficient of up to 0.82 × 10^6 cm^{-1}.[39] The HER in this work showed that an external potential lowers the reaction barriers and enhances this reaction under illumination.

Engineering the MoSSe monolayer's properties by combining it with other 2D vdW systems offers significant opportunities as well. For example, the MoSSe/$BiVO_4$ vdW heterostructure provides a clear demonstration that the Z-scheme (Fig. 4e) enables simultaneous HER and OER.[40] HSE06 calculations reveal that both monolayers have gaps of 2.09 eV and 3.24 eV, but when forming the heterostructure, the band gap decreases to 1.81 eV (visible-spectrum absorption), clearly indicating interaction between the monolayers.[40] The interaction between the two monolayers is confirmed by charge-transfer analysis, which shows that 0.078*e* are transferred from MoSSe to $BiVO_4$, generating a built-in field across the interface.[40] A key detail is shown in the band-edge analysis, where the MoSSe CBM is 0.61 eV above H^*/H_2, and $BiVO_4$ is about 1.76 eV below O_2/H_2O, potentially allowing both HER and OER reactions. The reaction potentials in the ΔG_{H^*} analysis are 0.98 for the HER and 2.62 for the OER, indicating improved HER but still inadequate OER (Fig. 4f),[40] with potentials similar to the case of MoSSe with N and F substitutions. Additionally, the Z-scheme heterostructure exhibits enhanced light absorption and improved carrier separation efficiency.

Another promising heterostructure is 2D black-P/MoSSe, in which black-P and MoSSe interact strongly, forming a vdW gap of just 2.18 Å and good lattice matching due to their minor 3.9% lattice mismatch.[41] In terms of electronic structure, it exhibits a type-II Z-scheme alignment with an indirect band gap of 0.79 eV, where the VBM derives from phosphorene and the CBM from MoSSe, and substantial offsets of 0.89 eV and 0.28 eV, respectively. The interaction between monolayers is not just vdW; it involves charge transfer from black-P to MoSSe, creating a potential drop of 0.45 eV and thus enhancing the Janus potential difference from 2.43 eV to 3.01 eV, and a dipole moment of the heterostructure of 2.56 D. As mentioned earlier, the strengthened polarization promotes efficient spatial separation of photocarriers. Another interesting effect in this vdW heterostructure is that the combined band edges straddle both the HER and OER redox potentials.[41] In this Z-scheme setup, black-P provides high-energy holes for the OER, while MoSSe supplies low-energy electrons needed for the HER, Fig. 4g. Combined with its broad optical response, including visible absorption around 500 nm and a high dielectric constant of 8.14,[41] it is likely that the black-P/MoSSe vdW heterostructure can overcome the inherent OER limitations of MoSSe to achieve complete water splitting.

Having seen that black-P/MoSSe has potential to drive the OER, we now describe another vdW heterostructure whose band edges straddle the redox potentials for water splitting as well. The first heterostructure is MoSSe/Ga_2SSe, whose most favorable configuration (formation energy of 0.69 eV) is achieved by stacking the monolayers *via* Se–Se bonds, with an interlayer spacing of 3.51 Å.[42] The heterostructure has a band gap of 2.02 eV and type-II alignment, with the VBM on MoSSe and the CBM on Ga_2SSe. It also depicts an interfacial potential step of 0.233 eV and charge transfer from Ga_2SSe to MoSSe that facilitates electron–hole separation. Also, the band edges straddle the HER and OER potentials under acidic conditions, but the alignment is lost at pH $>$ 4.5.[42] So, overall water splitting may occur under strongly acidic conditions. Another interesting characteristic is that the system absorbs across the visible spectrum, especially between 400–500 nm, and reaches a corrected solar-to-hydrogen efficiency of 10%.[42]

Other heterostructures with potential for the HER and OER at pH = 0 are MoSSe/GaN and MoSSe/AlN. In the heterostructures, the MoSSe layer sits atop the nitride hollow sites, minimizing repulsion. Evidence of this is the short vdW gap, 2.93 Å for MoSSe/GaN (formation energy -0.029 eV Å^{-2}) and 2.68 Å for MoSSe/AlN (formation energy -0.025 eV Å^{-2}).[43] Both systems display a type-II band alignment, yet with distinct band offsets. For MoSSe/GaN the CBM originates from MoSSe and the VBM originates from GaN, with band offsets of 1.480 eV and 0.377 eV, respectively.[43] A similar behavior is observed in MoSSe/AlN, where the CBM originates from MoSSe and the VBM from AlN, with band offsets of 2.294 eV and 0.352 eV, respectively.[43] The offsets indicate a unidirectional carrier flow in which electrons relax into the MoSSe CBM, while holes accumulate at either the GaN or AlN VBM. Such behavior is confirmed by analyzing charge densities and observing that GaN donates 0.107*e* and AlN donates 0.158*e* to MoSSe, generating strong interfacial fields with potential drops of 7.03 eV and 2.23 eV.[43] Both heterostructures straddle the HER and OER redox potentials at pH = 0, enabling them to promote both reactions, MoSSe being the reducing component and GaN/AlN the oxidizing component. The optical response of both heterostructures supports visible-light activity, with peaks near 425 nm (GaN) and 412 nm (AlN). Specifically, MoSSe/GaN features a high hole mobility (3476.81 cm^2 V^{-1} s^{-1}, 3651.83 cm^2 V^{-1} s^{-1}), making it particularly effective for the OER.[43]

In 2022, the MoSSe/GaN heterostructures were synthesized and tested under photoelectrochemical conditions,[44] providing a proof-of-concept of the quantum chemical predictions.[43] Computational calculations based on the experimental MoSSe/GaN system exhibit robust charge transfer from GaN to MoSSe (0.45*e*), rapid interfacial carrier extraction, and optical response in the 400–500 nm window.[44] Interestingly, the experiments reveal multifunctional behaviors that go beyond the known physical descriptors, including Rashba–Dresselhaus spin splitting, room-temperature ferromagnetic domains in MoSSe, and magnetically enhanced HER, characteristics not predicted by quantum-mechanical calculations.

Overall, the different MoSSe-based heterostructures exhibit a clear structure–function relationship in which interfacial dipoles, band alignment, and carrier transfer determine the system's ability to drive the full water-splitting reaction. As summarized in Table 1, the lateral junction MoSSe/WSSe relies on moderate polarization and type-II alignment to provide activity towards the HER and OER under acidic conditions. In contrast, Z-scheme stacks such as MoSSe/WS_2 or MoSSe/$BiVO_4$ exploit deeper valence bands to achieve strong oxidizing capabilities for the OER. Black-P/MoSSe stands out as the possible highest effective Z-scheme due to its strengthened interfacial dipole and broad absorption. On the other hand, in MoSSe/Ga_2SSe we observed that the redox alignment can be tuned by pH. Finally, in the nitride heterostructures, the large band offsets and strong built-in fields promote HER and OER activity in acidic conditions and fast hole/electron transport. Together, these systems show the viability of overcoming the MoSSe drawback for the OER by interfacing it with layers that complement its physical properties. Also, by interfacing MoSSe with the appropriate system, we can tune the physical descriptors to enable rational design of next-generation Janus-based photocatalysts.

Taken together, the body of work discussed here establishes a solid foundation for identifying the key physical descriptors governing photocatalytic water splitting in Janus MoSSe. A clear trend emerges in which pristine MoSSe and several engineered variants satisfy redox alignment and carrier separation requirements; however, only a limited subset of architectures combines these descriptors with thermodynamic and kinetic analyses for both HER and OER reactions. This reveals an important gap in the field, where many designs rely primarily on band-edge alignment, dipole enhancement, or optical absorption as proxies for activity, while reaction energetics, stability of the oxygenated intermediates and interface-specific

Table 1 Physical descriptors of MoSSe-based vdW heterostructures relevant for photocatalytic water splitting

Scheme	E_f, E_b	E_g (het)	Band edges *vs.* H^+/H_2 and O_2/H_2O (pH = 0 or 7)	HER/OER descriptors	Built-in field (ΔV)/dipole	Charge transfer (e)	Optical/STH	Ref.	WS
MoSSe/WSeS Type-II	E_f = −0.159 eV per cell	1.58 eV	CBM(MoSSe) 0.141 eV ↑ H^*/H_2 VBM(WSeS) 0.207 eV ↓ O_2/H_2O pH = 0	ΔG_H^* = 1.74 eV (MoSSe) ΔG_H^* = 1.81 eV (WSeS)	0.089 eV, 0.873 D	0.222 (WSeS → MoSSe)	Abs > 10^5 cm^{-1}	38	✓
MoSSe/WS_2 Z-scheme	E_b = −0.02 eV $Å^{-2}$	0.94 eV	CBM(MoSSe) straddle H^*/H_2 VBM(WS_2) straddle O_2/H_2O pH = 7	χ_H = 0.09, χ_O = 0.39	0.79 eV, —	—	Abs efficiency = 88.54%	39	✓
MoSSe/$BiVO_4$ Z-scheme	E_f = −0.02 eV $Å^{-2}$	1.81 eV	CBM(MoSSe) 0.61 eV ↑ H^*/H_2 VBM($BiVO_4$) 1.76 eV ↓ O_2/H_2O pH = 7	ΔG_H^* = 0.98 eV ΔG_{OER} = 2.62 eV	0.90 eV, —	0.222 (MoSSe → $BiVO_4$)	Abs from 413–689 nm	40	—
Black-P/MoSSe Z-scheme	—	1.28 eV	CBM(MoSSe) straddle H^*/H_2 VBM(black-P) straddle O_2/H_2O	—	0.45 eV, 2.56 D	not specified (BP → MoSSe)	Abs ≈ 500 nm	41	✓
MoSSe/Ga_2SSe Type-II	E_f = −0.69 eV per cell	2.02 eV	CBM(Ga_2 SSe) straddle H^*/H_2 VBM(MoSSe) straddle O_2/H_2O pH = 0	—	0.23 eV, —	0.024 (Ga_2 SSe → MoSSe)	Abs from 400–500 nm STH=10%	42	—
MoSSe/GaN Type-II	E_f = −0.029 eV $Å^{-2}$	1.48 eV	CBM(MoSSe) 1.48 eV ↑ H^*/H_2 VBM(GaN) 0.377 eV ↓ O_2/H_2O pH = 0	—	7.03 eV, —	0.107 (GaN → MoSSe)	Abs 425 nm	43	✓
MoSSe/AlN-Type-II	E_f = −0.025 eV $Å^{-2}$	1.42 eV	CBM(MoSSe) 2.294 eV ↑ H^*/H_2 VBM(AlN) 0.352 eV ↓ O_2/H_2O pH = 0	—	2.23 eV, —	0.158 (AlN → MoSSe)	Abs 425 nm	43	✓

✓: full overall water splitting; —: partial; + (none here): insufficient.

recombination channels are not consistently evaluated. The MoSSe/GaN system, which experimentally validated theoretical predictions based on the physical descriptors discussed here and also revealed additional effects such as spin splitting and magnetically enhanced reactions, demonstrates that descriptor-based design should preferably be complemented by thermodynamic analyses, reaction kinetics, and experimental operando validation. This integrated approach is particularly important for addressing the OER, identified throughout this perspective as the principal bottleneck for complete water splitting in MoSSe-based systems.

8 Practical challenges for MoSSe-based photocatalysts

Despite the rapid progress in understanding and engineering the photocatalytic properties of Janus MoSSe, several challenges must be addressed before these materials can be considered for practical solar fuel applications. In first place, the scalable and reproducible synthesis of high-quality Janus MoSSe and its heterostructures remains nontrivial, particularly for lateral heterostructures and defect-controlled architectures, where atomic-level precision is required to preserve the physical descriptors. In second place, long-term chemical and photostability under aqueous and illuminated conditions is still a field to explore, especially in the presence of reactive oxygenated intermediates during the OER.

Charge recombination at realistic interfaces, such as grain boundaries, substrate contacts, and imperfect heterojunctions, may also significantly affect the efficiencies predicted in the computational models and should be studied in detail.

While many studies report favorable band alignment and carrier separation, quantitative photocatalytic efficiencies under full solar illumination, including spectral losses and mass-transport effects, remain scarce. Addressing these challenges will require integrating descriptor-guided materials design with stability testing, operando spectroscopies, and device-level evaluations. Such efforts are essential to translate the fundamental insights discussed in this perspective into robust and efficient MoSSe-based photocatalytic systems.

9 Conclusions and future perspectives

In this perspective, we discussed MoSSe as a platform for understanding how built-in fields, dipole moments, band-edge asymmetry, charge transfer, optical properties, and related physical descriptors determine the photocatalytic applications. Pristine MoSSe has favorable charge separation and a suitable conduction band for the hydrogen evolution reaction, yet remains intrinsically limited for the oxygen evolution reaction because the S-side of the monolayer only weakly stabilizes oxygenated intermediates. Analysis of pristine multilayers, defect chemistry, transition-metal functionalization, co-doping, curvature, and van der Waals interfaces reveals that the best way to overcome this oxygen evolution reaction limitation is to exploit

interfacial polarization and band offsets either in Z-schemes or type-II configurations. Among these, vdW stacks are the best partners for enhancing the hole-driven oxygen evolution reaction while preserving the intrinsic hydrogen evolution activity on the MoSSe side. Nitride interfaces (GaN/MoSSe, AlN/MoSSe) are particularly promising, providing large internal fields, robust carrier separation, and band-edge positions that simultaneously fulfill both redox requirements. The experimental realization of the MoSSe/GaN heterostructure further confirms the predictive power of these theoretical descriptors, while also revealing additional multifunctional characteristics such as Rashba–Dresselhaus splitting and magnetic-field-enhanced charge dynamics, as non-conventional physical descriptors.

MoSSe should be considered as a tunable building block whose dipole, carrier lifetimes, and interfacial chemistry can be rationally engineered for complete water splitting. Future progress relies on explicitly resolving OER pathways in new 2D Janus-based architectures and on integrating operando spectroscopies with quantum-mechanical calculations to track reaction intermediates under realistic conditions. Such efforts may refine the design principles identified here and accelerate the development of Janus-based heterostructures for efficient, visible-light-driven solar conversion.

Conflicts of interest

There are no conflicts to declare.

Data availability

No primary research results, software or code have been included and no new data are generated or analysed as part of this perspective.

Acknowledgements

We thank DGAPA-UNAM project IG101124 for partial financial support. JGS acknowledges the LVMM group for all the useful scientific discussions. JGS acknowledges the CNyN's P-Table for all the great moments and useful discussions.

References

1 X. Zhang, Z. Lai, Q. Ma and H. Zhang, *Chem. Soc. Rev.*, 2018, **47**, 3301–3338.
2 A. Rawat, M. K. Mohanta, N. Jena, Dimple, R. Ahammed and A. De Sarkar, *J. Phys. Chem. C*, 2020, **124**, 10385–10397.
3 M. Idrees, H. U. Din, R. Ali, G. Rehman, T. Hussain, C. V. Nguyen, I. Ahmad and B. Amin, *Phys. Chem. Chem. Phys.*, 2019, **21**, 18612–18621.
4 A. C. Riis-Jensen, T. Deilmann, T. Olsen and K. S. Thygesen, *ACS Nano*, 2019, **13**, 13354–13364.
5 T. Hu, F. Jia, G. Zhao, J. Wu, A. Stroppa and W. Ren, *Phys. Rev. B*, 2018, **97**, 235404.
6 J. Jiang and W. Mi, *Mater. Horiz.*, 2023, **10**, 788–807.
7 J. He and S. Li, *Comput. Mater. Sci.*, 2018, **152**, 151–157.
8 D. B. Trivedi, G. Turgut, Y. Qin, M. Y. Sayyad, D. Hajra, M. Howell, L. Liu, S. Yang, N. H. Patoary, H. Li, M. M. Petric, M. Meyer, M. Kremser, M. Barbone, G. Soavi, A. V. Stier, K. Müller, S. Yang, I. S. Esqueda, H. Zhuang, J. J. Finley and S. Tongay, *Adv. Mater.*, 2020, **32**, 2006320.
9 D. Er, H. Ye, N. C. Frey, H. Kumar, J. Lou and V. B. Shenoy, *Nano Lett.*, 2018, **18**, 3943–3949.
10 W.-J. Yin, H.-J. Tan, P.-J. Ding, B. Wen, X.-B. Li, G. Teobaldi and L.-M. Liu, *Mater. Adv.*, 2021, **2**, 7543–7558.
11 Y.-C. Lin, C. Liu, Y. Yu, E. Zarkadoula, M. Yoon, A. A. Puretzky, L. Liang, X. Kong, Y. Gu, A. Strasser, H. M. Meyer, M. Lorenz, M. F. Chisholm, I. N. Ivanov, C. M. Rouleau, G. Duscher, K. Xiao and D. B. Geohegan, *ACS Nano*, 2020, **14**, 3896–3906.
12 A.-Y. Lu, H. Zhu, J. Xiao, C.-P. Chuu, Y. Han, M.-H. Chiu, C.-C. Cheng, C.-W. Yang, K.-H. Wei, Y. Yang, Y. Wang, D. Sokaras, D. Nordlund, P. Yang, D. A. Muller, M.-Y. Chou, X. Zhang and L.-J. Li, *Nat. Nanotechnol.*, 2017, **12**, 744–749.
13 M. Liu, W. Wu, Z. Chen, Y. Zhang, X. Yu, S. Yang, H. Wang, F. Xu, L. Chen, X. Li, Y. Wu, Z. Wu and J. Kang, *Nano Lett.*, 2025, **25**, 5723–5730.
14 A. L. P. Sino, T.-W. Lin, S. Wani, L.-S. Lee, C.-A. Chen, M.-H. Liu, Y.-H. Kuo, B. Rehman, K. T. Le, J.-Y. Wu, F.-C. Chuang and Y.-L. Chueh, *Mater. Today*, 2023, **69**, 97–106.
15 X. Zheng, K. Zhang, X. Zhao, J. Zhou, H. Shen, J. Kong and Y. Guo, *ACS Nano*, 2025, **19**, 20744–20752.
16 C. W. Jang, W. J. Lee, J. K. Kim, S. M. Park, S. Kim and S.-H. Choi, *NPG Asia Mater.*, 2022, **14**, 15.
17 Y. Qin, M. Sayyad, A. R. Montblanch, M. S. G. Feuer, D. Dey, M. Blei, R. Sailus, D. M. Kara, Y. Shen, S. Yang, A. S. Botana, M. Atature and S. Tongay, *Adv. Mater.*, 2021, **34**, 2106222.
18 J. Schmeink, J. Osterfeld, O. Kharsah, S. Sleziona and M. Schleberger, *npj 2D Mater. Appl.*, 2024, **8**, 67.
19 Z. Gan, I. Paradisanos, A. Estrada-Real, J. Picker, E. Najafidehaghani, F. Davies, C. Neumann, C. Robert, P. Wiecha, K. Watanabe, T. Taniguchi, X. Marie, J. Biskupek, M. Mundszinger, R. Leiter, U. Kaiser, A. V. Krasheninnikov, B. Urbaszek, A. George and A. Turchanin, *Adv. Mater.*, 2022, **34**, 2205226.
20 J. Picker, M. Ghorbani-Asl, M. Schaal, S. Kretschmer, F. Otto, M. Gruenewald, C. Neumann, T. Fritz, A. V. Krasheninnikov and A. Turchanin, *Nano Lett.*, 2025, **25**, 3330–3336.
21 N. Bokka, S. K. Ganeshan and P. Sahatiya, *Flexible Printed Electron.*, 2021, **6**, 015011.
22 T. Hisatomi and K. Domen, *Nat. Catal.*, 2019, **2**, 387–399.
23 T. Hisatomi, J. Kubota and K. Domen, *Chem. Soc. Rev.*, 2014, **43**, 7520–7535.
24 A. Fujishima and K. Honda, *Nature*, 1972, **238**, 37–38.
25 S. Chen, T. Takata and K. Domen, *Nat. Rev. Mater.*, 2017, **2**, 17050.
26 J. I. Paez-Ornelas, R. Ponce-Pérez, H. N. Fernández-Escamilla, D. M. Hoat, E. A. Murillo-Bracamontes, M. G. Moreno-Armenta, D. H. Galván and J. Guerrero-Sánchez, *Sci. Rep.*, 2021, **11**, 21061.

27 C.-F. Fu, Q. Zheng, X. Li and J. Yang, *Nano Lett.*, 2024, **24**, 6425–6432.
28 X. Ma, X. Wu, H. Wang and Y. Wang, *J. Mater. Chem. A*, 2018, **6**, 2295–2301.
29 X. Lei, C. Ouyang and K. Huang, *Appl. Surf. Sci.*, 2021, **537**, 147919.
30 W.-J. Yin, B. Wen, G.-Z. Nie, X.-L. Wei and L.-M. Liu, *J. Mater. Chem. C*, 2018, **6**, 1693–1700.
31 Z. Guan, S. Ni and S. Hu, *J. Phys. Chem. C*, 2018, **122**, 6209–6216.
32 Y. Xu, Y. Yao, W. Yin, J. Cao, M. Chen and X. Wei, *RSC Adv.*, 2020, **10**, 10816–10825.
33 X. Ma, X. Yong, C.-c Jian and J. Zhang, *J. Phys. Chem. C*, 2019, **123**, 18347–18354.
34 Y.-M. Zhao, P. Ren, X.-Y. Ma, J. P. Lewis, Q.-B. Yan and G. Su, *J. Phys. Chem. C*, 2021, **125**, 11939–11949.
35 F. Zhao, J. Li, Y. Chen, M. Zhang and H. Zhang, *Appl. Surf. Sci.*, 2021, **544**, 148741.
36 S. Zhang, H. Jin, C. Long, T. Wang, R. Peng, B. Huang and Y. Dai, *J. Mater. Chem. A*, 2019, **7**, 7885–7890.
37 J. Zhang, X. Tang, M. Chen, D. Ma and L. Ju, *Inorg. Chem.*, 2022, **61**, 17353–17361.
38 X. Yang, J. P. Wärnå, J. Wang, P. Zhang, W. Luo and R. Ahuja, *J. Catal.*, 2021, **404**, 18–31.
39 N. T. G. Bao, T. N. Q. Trang, N. Thoai, T. B. Phan, V. T. H. Thu and N. Tuan Hung, *ACS Appl. Energy Mater.*, 2025, **8**, 5209–5221.
40 W. Chen, J. Yang, Y. Zhu, Y. Zhang, Y. Zhao, Y. Wen and B. Liang, *J. Phys. D: Appl. Phys.*, 2022, **55**, 305501.
41 G. Wang, C. Chen, B. S. Teketel, B. Xu and B. Lin, *Int. J. Hydrogen Energy*, 2021, **46**, 39183–39194.
42 F. Yang, P. Boulet and M.-C. Record, *Int. J. Hydrogen Energy*, 2024, **73**, 536–546.
43 K. Ren, S. Wang, Y. Luo, J.-P. Chou, J. Yu, W. Tang and M. Sun, *J. Phys. D: Appl. Phys.*, 2020, **53**, 185504.
44 D. Ghosh, K. Roy, S. Maitra and P. Kumar, *J. Phys. Chem. Lett.*, 2022, **13**, 1234–1240.